Engineering Failure Analysis 163 (2024) 108529

Contents lists available at ScienceDirect

Engineering Failure Analysis

journal homepage: www.elsevier.com/locate/engfailanal

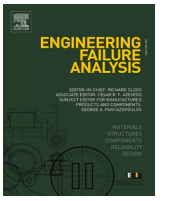

Failure analysis of hybrid Aluminium-to-Steel welded joints under Uniaxial/Multiaxial fatigue loading

Chin Tze Ng , Luca Susmel *

Department of Civil and Structural Engineering, The University of Sheffield, Mappin Street, Sheffield S1 3JD, UK

ARTICLE INFO

Keywords:
Aluminium-to-steel welded joints
Fatigue crack initiation and propagation
Multiaxial fatigue

ABSTRACT

This paper conducts a comprehensive crack path analysis of hybrid aluminium-to-steel welded joints fabricated using EWM coldArc® welding technology, focusing on uniaxial/multiaxial fatigue loading conditions. Following fatigue failure of the specimens under investigation, detailed examination of the crack initiation and propagation phases was performed, with particular attention to the crucial role of crack initiation in failure under multiaxial fatigue loading. Through crack path analysis, four primary crack initiation locations were identified across uniaxial, pure torsional, and biaxial fatigue loading scenarios, i.e., weld toe, weld start/stop position, weld itself, and the aluminium heat-affected zone (HAZ). Results indicate that the weld toe region is the predominant site of crack initiation, especially under uniaxial and biaxial constant amplitude fatigue loading. However, under specific loading conditions, crack initiation shifts towards the weld start/stop position, possibly due to localised stress concentration effects induced by weld geometry. Remarkably, cracks originating from the weld itself were relatively uncommon, underscoring the effectiveness of EWM cold arc technology in welding thin dissimilar aluminium-to-steel connections. Additionally, crack plane orientation analysis revealed shear stresses as governing crack initiation and normal stresses as controlling crack propagation. Experimental and theoretical crack plane orientations demonstrated close correlation, with crack initiation angle error mainly within ± 20 % of the maximum shear stress plane angle and crack propagation angle error mainly within ± 30 % of the maximum normal stress angle. This study offers valuable insights into the behaviour of such joints under multiaxial fatigue loading, with potential implications for enhancing their structural integrity and reliability in engineering applications.

1. Introduction

Welding technologies capable of joining dissimilar materials have received considerable attention in the fabrication of light, economic and environmentally sustainable structural assemblies. One of the main goals of manufacturing is to obtain ideal mechanical properties from both materials simultaneously, while also reducing the weight and cost of structural components. This is achieved by integrating load-bearing steel components with aluminium elements, taking advantage of aluminium's lighter weight and greater recyclability without sacrificing the strength of the material. This reduction in the weight of the vehicle not only improves fuel efficiency but also offers a sustainable approach to reducing carbon emissions [1–3]. Significantly, these advantages extend beyond automotive applications to the construction and structural sectors.

* Corresponding author.
E-mail address: l.susmel@sheffield.ac.uk (L. Susmel).

https://doi.org/10.1016/j.engfailanal.2024.108529
Received 5 April 2024; Received in revised form 18 May 2024; Accepted 3 June 2024
Available online 5 June 2024

Nomenclature

σ_a	Nominal normal stress amplitude
τ_a	Nominal shear stress amplitude
λ	Biaxiality stress ratio
R	Load ratio (i.e., R = -1, 0.1)
$A_{ini,exp}$	Experimental crack initiation angle
$A_{pro,exp}$	Experimental crack propagation angle
$A_{ini,theo}$	Theoretical crack initiation angle derived from Mohr's circle
$A_{pro,theo}$	Theoretical crack propagation angle derived from Mohr's circle
PSBs	Persistent slip bands
E	Percentage error between experimental and theoretical angles
HAZ	Heat affected zone in welding

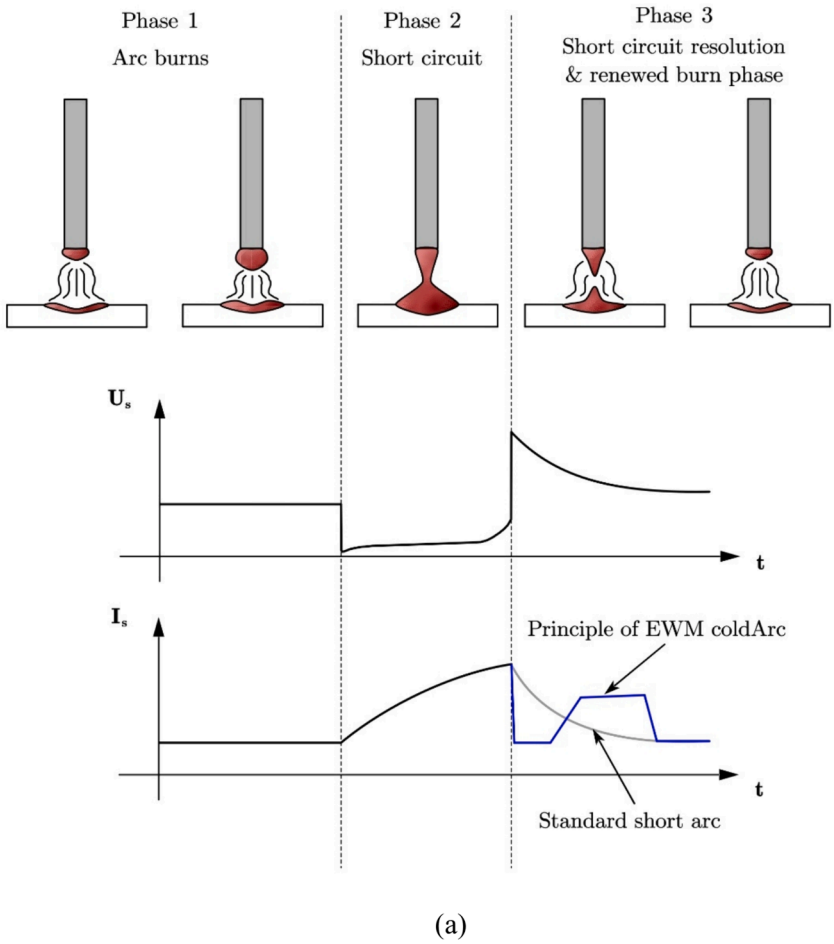

Fig. 1. Principle and advantages of EWM coldArc® welding during arc reignition phase: (a) waveform voltage and current, (b) reduction in power output.

Nonetheless, welding aluminium to steel has always been challenging due to their significant differences in mechanical, thermo-physical, and metallurgical characteristics, often resulting in the formation of a brittle intermetallic (Fe-Al) phase within the weld region [1–7]. To address this issue, various welding technologies have been developed, including laser beam welding, explosion welding, friction stir welding, laser pulse welding, magnetic pulse welding, and coldArc® welding [1–3,8–11]. Among these technologies, the recently optimised EWM coldArc® welding method has been selected for interest as it is the preferred welding technology

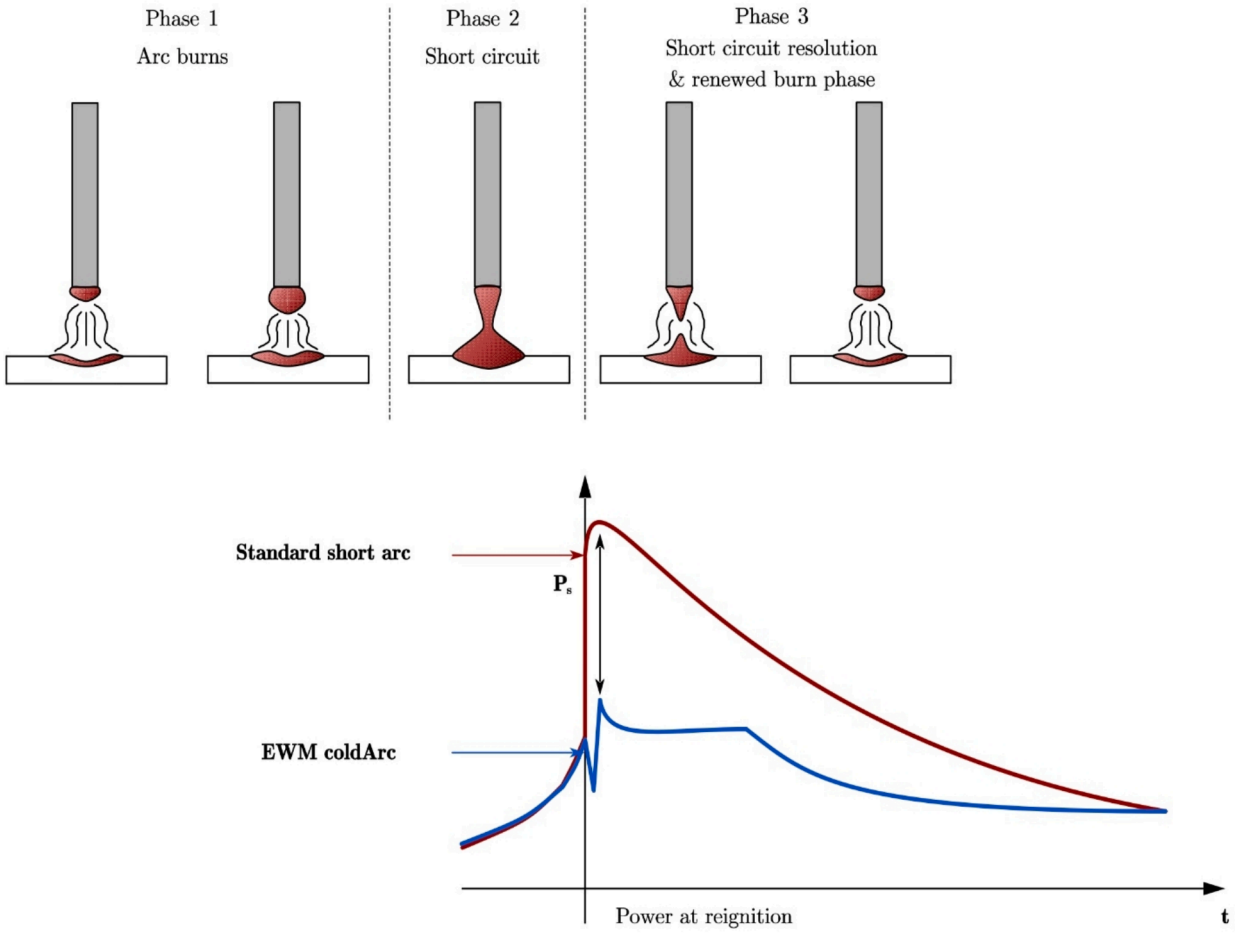

(b)

Fig. 1. (*continued*).

for producing hybrid steel and aluminium welded specimens discussed in this study [3,5].

The EWM coldArc® welding, commercialised by EWM Hightec Welding GmbH, offers precise control of heat input and metal transfer without mechanical intervention in the wire feed process. This modified low-energy short arc process enables successful welding of thin metal sheets without burn-through, accommodating sheets as thin as 0.3 mm with automated welding machines and 0.7 mm with manual welding machines. Furthermore, its effectiveness in welding mixed joints, including aluminium to steel, has been demonstrated in previous studies [3,5,6,10].

To ensure robust joint strength in the hybrid aluminium-to-steel welded joints, attention is directed to the Fe-Al phase diagram, revealing the lack of solubility between iron or steel and aluminium [3,5,7,8,12]. To prevent the formation of brittle intermetallic Fe-Al phases, which can occur when the proportion of Fe-Al phases in the molten material exceeds 10 %, zinc coating is applied to the surface of the steel tubular part [3,5,7,8,12]. This technique facilitates the formation of a strong joint between steel and aluminium by partially melting the aluminium during welding while only moistening the steel to prevent brittleness from the molten material, resulting in a welded joint on one side and a brazed joint on the other [3,5].

In particular, Fig. 1a illustrates the waveform of both conventional and cold arc processes. While the initial two phases of the welding process resemble those of conventional arc welding, the third phase stands out for its dynamic control over current output during arc re-ignition [3,5]. With a consistent voltage profile resembling the short arc process, rapid adjustments are made for optimal regulation, facilitated by a digital signal processor, as depicted in Fig. 1a [3,5]. This refined re-ignition process ensures immediate molten material formation on the electrode tip, followed by a brief melt pulse period to ensure uniform electrode melting and prevent excessive melting [3,5,10]. The significant reduction in power peak during arc re-ignition in the EWM cold arc welding method, as illustrated in Fig. 1b, underscores its advantages, including minimal spatter formation, reduced panel thickness minimal material distortion, and damage to zinc coating, along with effective gap bridging capabilities [3,5,6].

Table 1
Parameters for EWM cold arc® welding.

Welding Settings	
Program	Pulse 224
Arc Voltage	12.6 V
Current	40 A
Wire Feed Rate	2.8 m/min
Weld Speed	3.27 mm/s

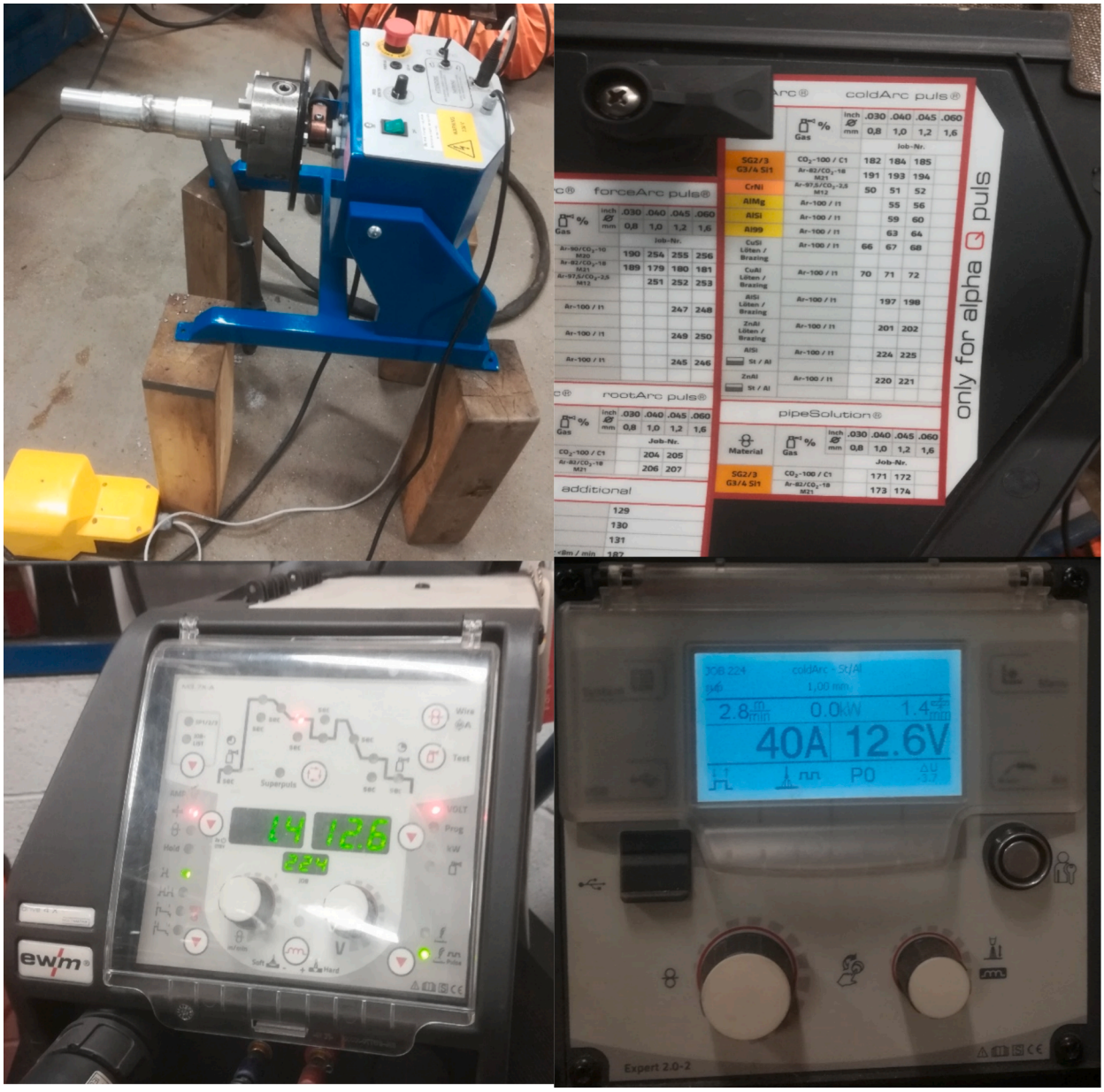

Fig. 2. Setup and interface of the EWM alpha Q551 pulse welding machine.

Moreover, it is noteworthy that the welding parameters are optimised and incorporated into the machine program provided by the welding company EWM. By selecting the appropriate program code from the provided list and specifying the material thickness, the machine configures the corresponding welding parameters accordingly. The optimised EWM coldArc® welding parameters used to fabricate the tube-tube hybrid aluminium to steel welded joint samples in this study are summarised in Table 1. The specimens under

Table 2
Chemical composition of investigated materials by weight percentage (%).

Material	Chemical Composition (wt%)								
	Mg	Si	Mn	Fe	Zn	Cu	Ti	Cr	Al
AA6082-T6	0.60–1.20	0.70–1.30	0.40–1.00	0.50	0.20	0.10	0.10	0.25	Balance
S235	Mn	C	P	S					
	1.40 (max)	0.20 (max)	0.035 (max)	0.035 (max)					
AWS A5.10 ER4043	Mg	Si	Mn	Fe	Zn	Cu	Ti	Al	
	0.05 (max)	4.5–6.0	0.05 (max)	0.80 (max)	0.10 (max)	0.30 (max)	0.20 (max)	Balance	

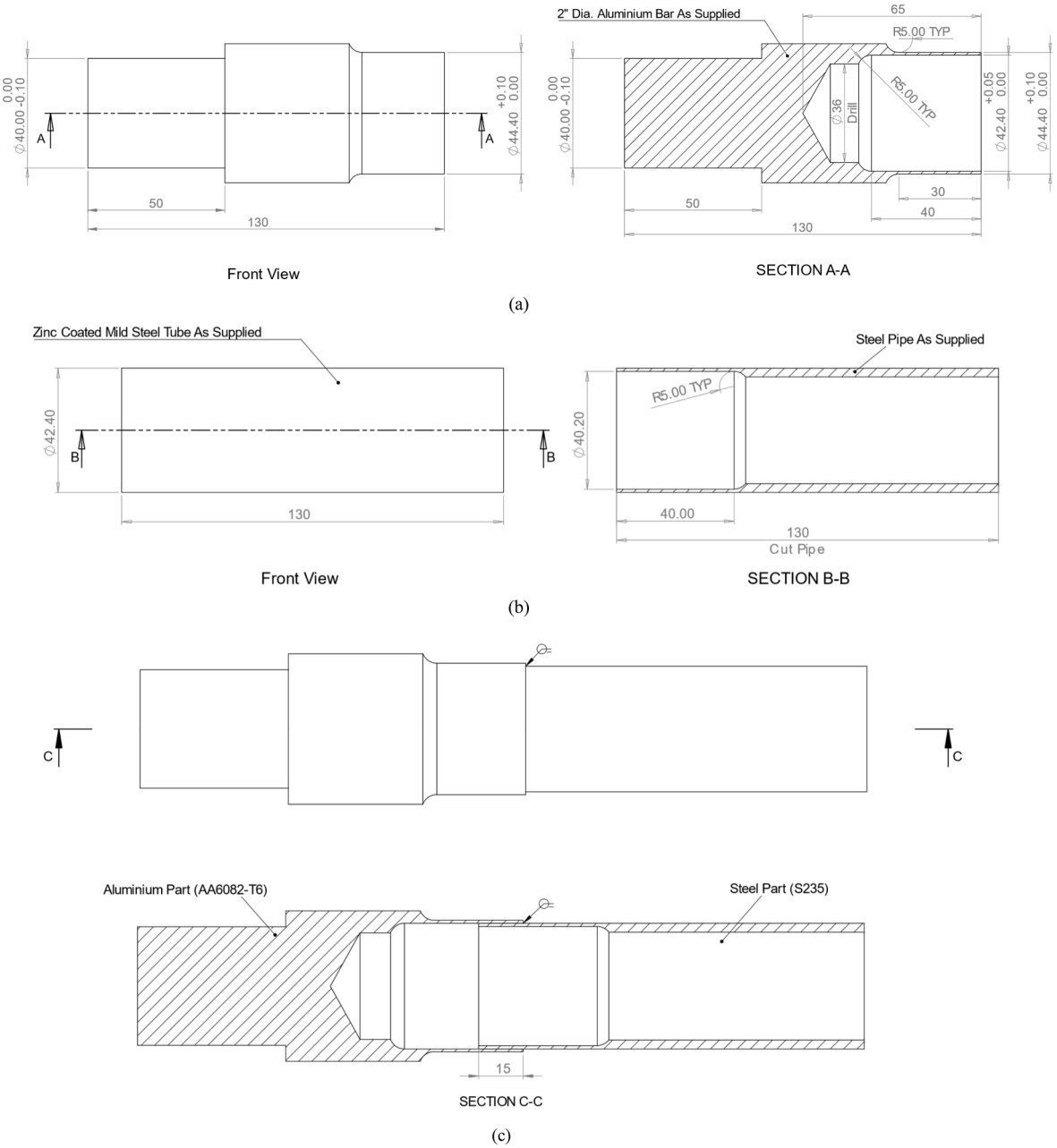

Fig. 3. Geometrical configuration of the investigated hybrid aluminium-to-steel welded joint samples: (a) aluminium (AA6082-T6) part, (b) steel (S235) part, and (c) complete hybrid welded joint.

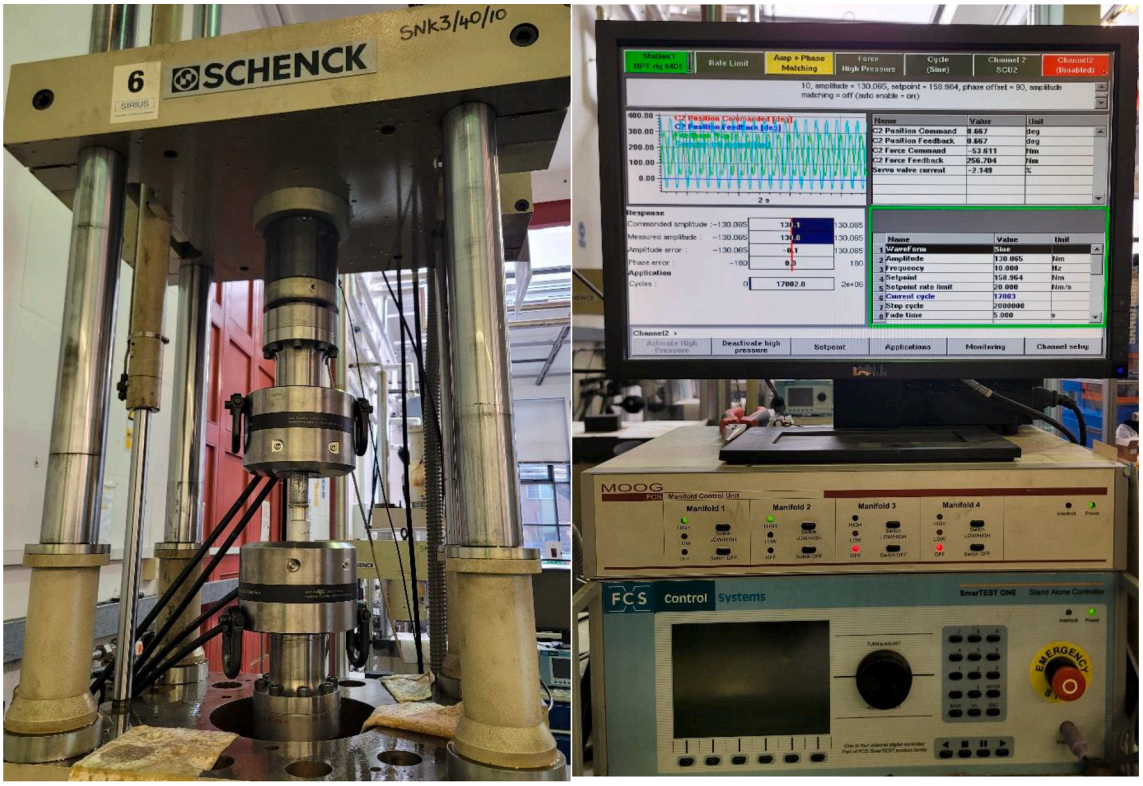

(a) (b)

Fig. 4. Experimental setup for fatigue testing: (a) Schenck servohydraulic tension–torsion fatigue machine, (b) FCS SmarTEST ONE Servo Controller.

investigation were manually welded together by an experienced technician. Further insights into the setup and interface of the EWM alpha Q551 pulse welding machine for the coldArc® welding process are illustrated in Fig. 2.

Additionally, the susceptibility of welded joints to fatigue failure presents another significant challenge. The examined references collectively contribute to the understanding of welding and fatigue behaviour across various materials and joint configurations. For instance, studies on aluminium-to-steel welded joints under static loading [6] and the fracture mechanisms of aluminium-to-steel laser arc welded brazed joints under varied conditions [13] offer crucial insights into hybrid and dissimilar metal welding. Similarly, research on dissimilar aluminium alloys friction stir welded with additively manufactured tools [14] sheds light on microstructure and welding interfaces under tension, contributing to the understanding of hybrid joints.

Extensive research have been conducted on crack path analysis, with research focusing on crack initiation and propagation paths in various types of welded joints, including tubular, fillet weld, tube-flange, and cruciform joints, predominantly under tension, torsion, and bending loadings [15–21]. Investigations into stress analysis approaches and fatigue life prediction to examine the accuracy of different stress analysis approaches in assessing the fatigue lifetime of steel and aluminium welded joints under multiaxial fatigue loading were also performed [22–25].

Despite the breadth of research, a notable gap persists in studies specifically addressing crack path analysis of thin hybrid aluminium-to-steel welded joints under multiaxial fatigue loading. This study aims to address this knowledge gap by presenting our findings and analysis on this matter.

2. Experimental procedure

In this study, aluminium alloy AA6082 T6 and zinc coated S235 steel, compliant to EN 10255 standards, were adopted. The chosen filler material was AWS A5.10 ER4043. A summary of the chemical composition and mechanical properties of these materials can be found in Table 2, while detailed drawings of the specimen geometrical configuration are provided in Fig. 3. Specifically, the weld intersection region involved overlapping 1 mm thick hollow tubular aluminium with 1 mm thick galvanised hollow tubular steel. Meticulous alignment during the welding process ensured a seamless fit between the steel and aluminium parts, enabling them to fit nicely into the grips and preventing undesirable eccentric loading effects.

Fatigue tests were conducted at room temperature using a Schenck servohydraulic tension–torsion fatigue testing machine, with

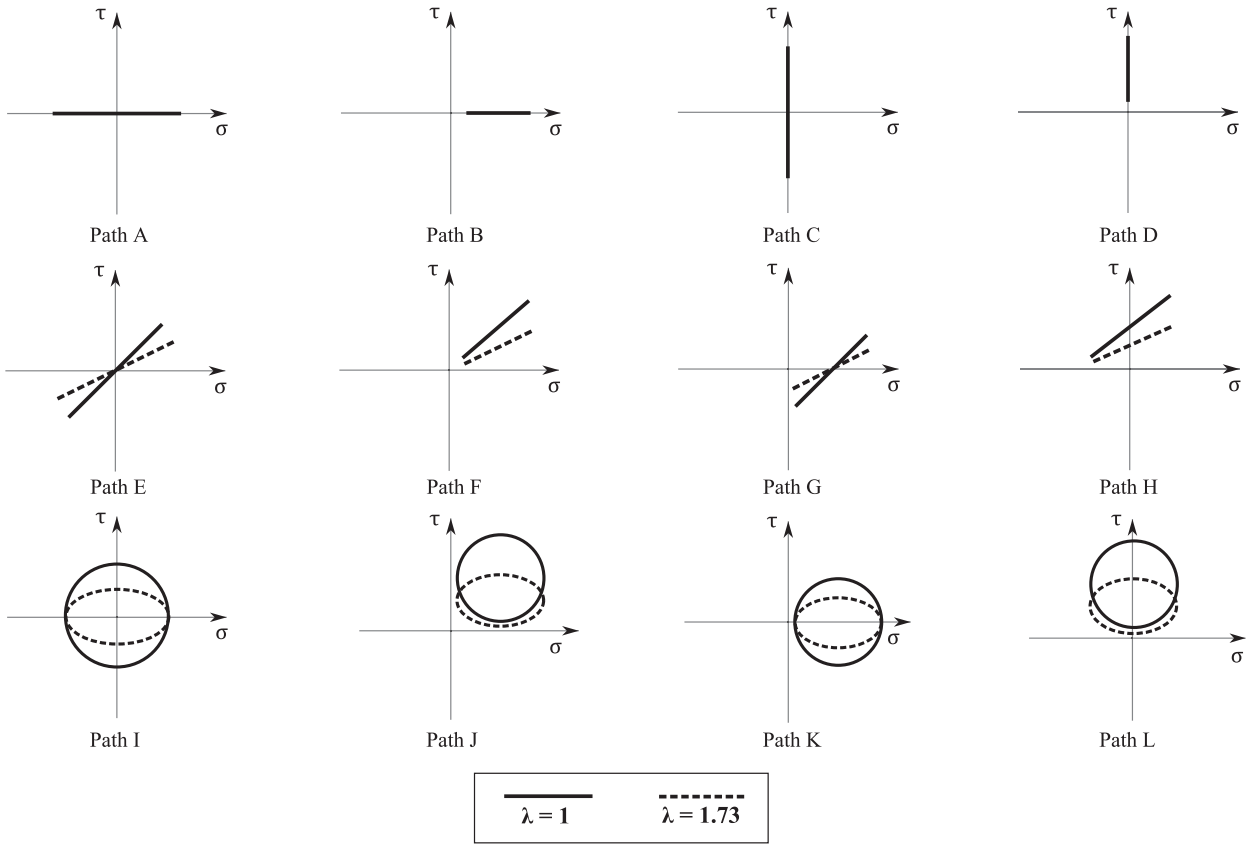

Fig. 5. Investigated fatigue loading paths.

Table 3
Fatigue testing matrix including loading paths, biaxiality ratio (λ), and number of samples.

Load Type	Loading Path	Biaxiality ratio, λ	No. of Samples	Total No. of Samples
Uniaxial	A	∞	8	12
	B	∞	4	
Pure Torsion	C	0	8	12
	D	0	4	
Biaxial	E	1	6	72
		1.73	6	
	F	1	4	
		1.73	4	
	G	1	4	
		1.73	4	
	H	1	4	
		1.73	4	
	I	1	6	
		1.73	6	
	J	1	4	
		1.73	4	
	K	1	4	
		1.73	4	
	L	1	4	
		1.73	4	

the FCS SmarTEST ONE Servo Controller controlling the fatigue loadings through various channels as depicted in Fig. 4. Throughout the fatigue testing, hybrid aluminium-to-steel welded joint samples were securely clamped in place using an MTS 646 Hydraulic Collet Grip, capable of withstanding a maximum pressure of 45 MPa, with 250kN axial load capacity and 2200Nm torsional capacity. Due to

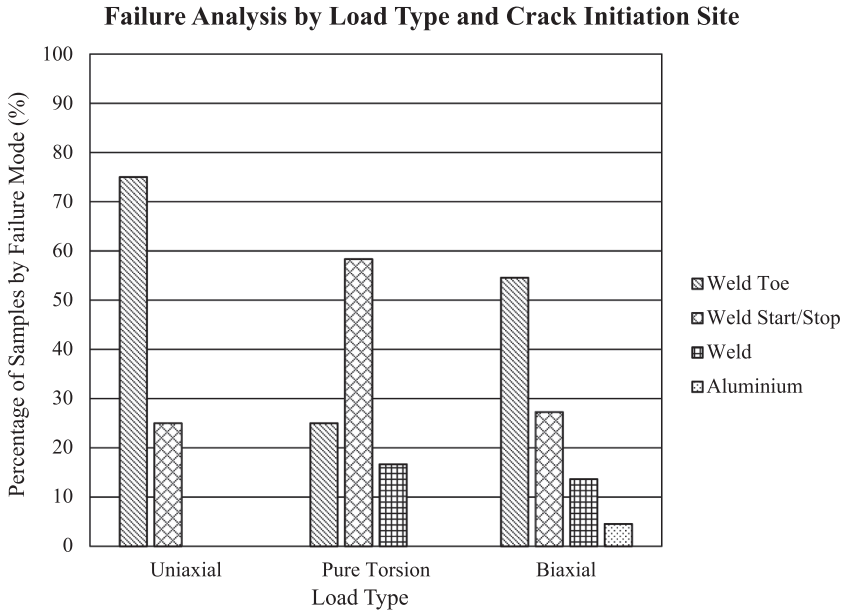

Fig. 6. Analysis of crack initiation locations by fatigue loading type.

the collet grip's 40 mm maximum diameter, the specimens were tailored with a non-standard hollow tube-tube geometry to accommodate grip limitations, with the grips spaced 140 mm apart while clamping the specimens.

The specimens were tested in their as-welded condition, i.e., without undergoing any heat treatment before mechanical testing. It is worth noting that the selected welded joints were carefully chosen to ensure high quality, with specimens free from visible spatter, pores, or cracks being excluded from testing. To assess the mean stress effect, loading ratios, R of −1 and 0.1 were employed, alongside biaxial fatigue tests conducted both in phase and 90° out of phase, employing sinusoidal constant amplitude loading at a frequency of 10 Hz. Loading path diagrams of the fatigue tests are illustrated in Fig. 5. For research and development purposes, it was advised to conduct 6 to 12 tests for each test series, with a minimum of 2 samples per stress level, resulting in a minimum of 8 samples tested for all primary tests with an R of −1, and at least 2 repetitions for each stress amplitude level, ensuring a replication level of 50 % which aligns with the minimum 33 % replication percentage as recommended in ASTM E739-10 [26].

The biaxiality stress ratio, λ, was calculated through the amplitude of the axial stress, σ_a, and the amplitude of the torsional stress, τ_a, as follows:

$$\lambda = \frac{\sigma_a}{\tau_a} \tag{1}$$

During fatigue testing, stress ratio λ was fixed at 1 and $\sqrt{3}$ to assess its impact on the critical plane and fatigue life. The fatigue testing matrix summarised in Table 3 consists of different loading configurations, including uniaxial, pure torsion, and biaxial tests, outlining loading paths and the corresponding number of tested welded joint samples. Nominal normal stress amplitudes ranging from 30 to 85 MPa were applied, resulting in fatigue test durations spanning from 10^3 to 2 million cycles to failure, aligning with the medium to high fatigue regime of interest in this study. Runout was defined at 2 million cycles and specimens were retested at higher stress amplitudes.

The termination criterion for the fatigue tests was a 10 % reduction in material stiffness, coinciding with the appearance of visible cracks measuring between 10 to 20 mm in length. This reduction in stiffness was indicative of a loss of mechanical strength and functionality as a safe structural element. The number of cycles to failure was recorded accordingly. Notably, it is essential to clarify that these nominal normal and shear stresses are determined with reference to the surface area of the aluminium tube at the critical welding region, rather than the steel tube. Lastly, the cracking behaviour and paths of the examined hybrid welded joints were analysed, as discussed in the following section.

3. Crack path analysis

The fatigue failure process typically progresses through two different stages: crack initiation phase (Stage I) and crack propagation phase (Stage II) [16,17,20,27–35]. This analysis focuses on the crucial early phases of crack formation and growth, with a specific emphasis on crack initiation, given its significant influence on the failure of hybrid welded joints under fatigue loading. The crack path analysis in this investigation was primarily conducted at a mesoscopic to macroscopic scale, utilising front and plan views to identify the crack initiation site and surface, respectively.

In what follows, the crack path analysis of the hybrid joints under investigation will be approached from two different perspectives. Firstly, the crack initiation location will be examined, taking into account the different types of fatigue loading. Then, an analysis of the

Fig. 7. Crack initiation under uniaxial loading: (a) from weld toe, (b) from weld start/stop position.

orientation of both crack initiation and propagation planes will be conducted.

3.1. Crack initiation site

The crack path analysis reveals that crack initiation only occurs from a single localised point in most samples regardless of both the

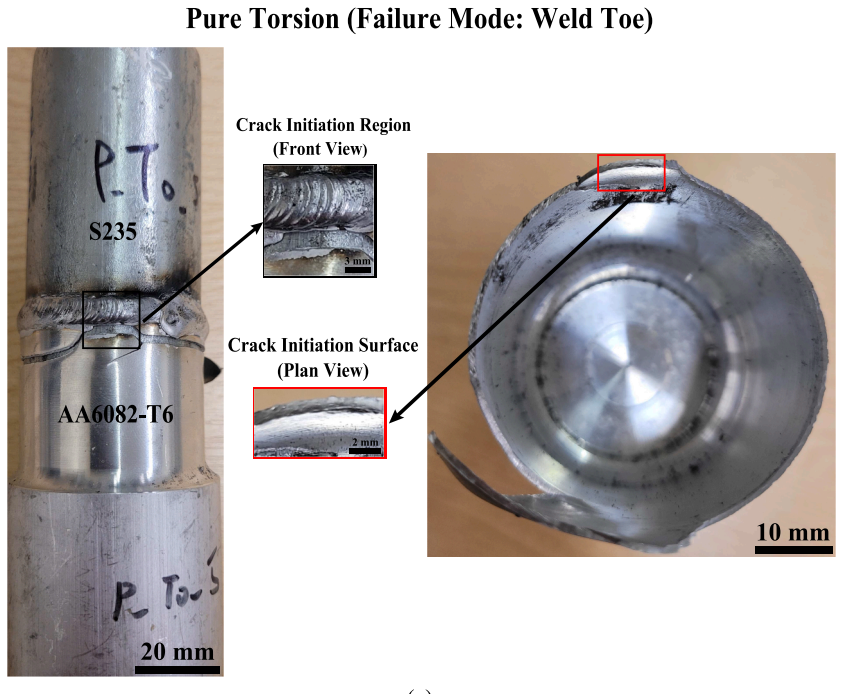

Fig. 8. Crack initiation under pure torsional loading: (a) from weld toe, (b) from weld start/stop position, and (c) from the weld itself.

type of fatigue loading and level of stress amplitudes. In a perfectly ideal scenario, this initiation point is random, as nominal stresses are evenly distributed around the tube-tube welded joints. However, complications start to arise when stress concentration effects, arising from localised geometric features introduced by the weld start/stop and weld toe position become more pronounced, ultimately dictating the failure mode. The analysis identifies four different crack initiation locations influencing the failure mode of the hybrid joints, which are the weld toe, weld start/stop position, weld itself, and the heat-affected zone (HAZ) of the aluminium. These initiation sites are depicted in the legend of the bar chart showcased in Fig. 6. Each fatigue loading type will be depicted by illustrating observed crack initiation sites, offering examples for each failure mode case. Furthermore, based on the crack path analysis, no clear correlation exists between the crack initiation site and the level of the applied stress amplitudes during fatigue testing.

The bar chart in Fig. 6 reveals a clear correlation between load type and the percentage of samples exhibiting specific failure modes. Under uniaxial fatigue loading, the predominant site of crack initiation is the weld toe, with 75 % of specimens displaying cracks

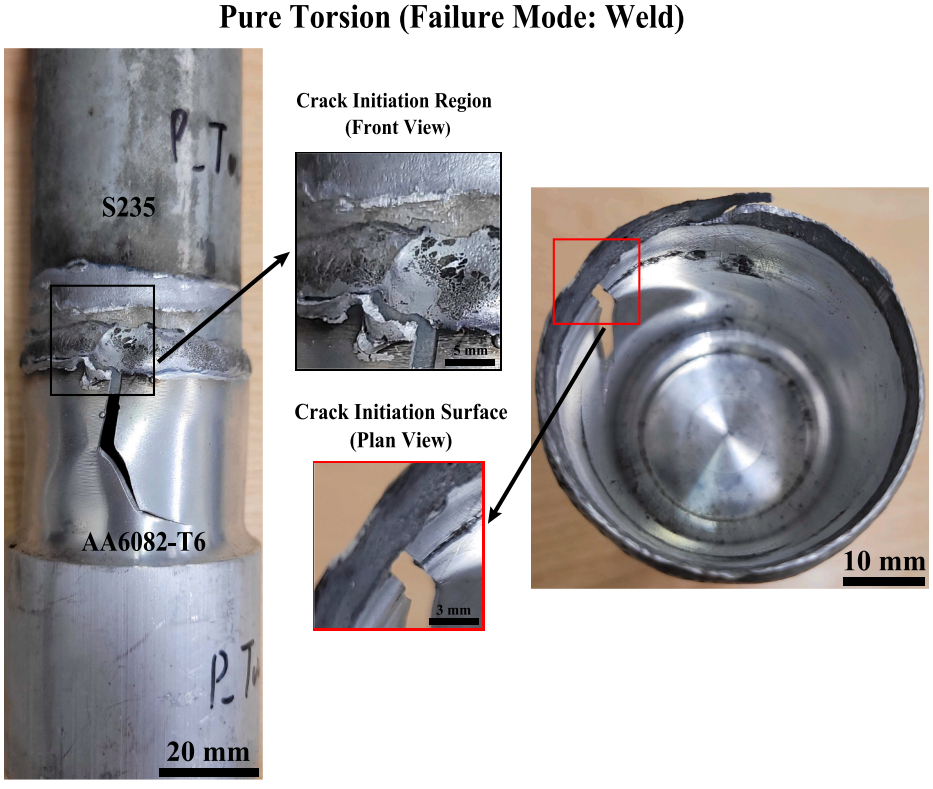

(c)

Fig. 8. (*continued*).

originating from this location. Fig. 7a provides a visual representation of cracks initiating from the weld toe position in this loading scenario. Conversely, a minority of 25 % of samples show cracks initiating from the weld start/stop position, as illustrated in Fig. 7b.

In the context of pure torsional fatigue loading, Fig. 8a provides an illustration of cracks originating from the weld toe position. In Fig. 8b, cracks are observed to begin from the weld start/stop position, characterised by a noticeable bulge in the weld pool. Additionally, Fig. 8c showcases cracks initiating directly from the weld itself, resulting in detachment from the tubular samples. Analysis indicates that the majority of specimens, approximately 58 %, experience failure from the weld start/end position, while 25 % fail from the weld toe position, with only a minority of 17 % exhibiting failure from the weld itself.

Shifting our attention to biaxial fatigue loading scenarios, which encompass both in-phase and out-of-phase constant amplitude fatigue loading, as well as tests with varying λ, four primary sites of crack initiation were identified. These sites include the weld toe, weld start/stop position, weld itself, and the HAZ of the aluminium. In Fig. 9a, the majority of failures, accounting for 55 % of samples, are attributed to cracks originating at the weld toe. Fig. 9b illustrates crack initiation from the weld start/stop position, representing 27 % of observed samples. In Fig. 9c, cracks are observed to initiate directly from the weld, a mode of failure observed in only 14 % of specimens. Lastly, as depicted in Fig. 9d, cracks are found to originate from the aluminium HAZ, a rare occurrence observed in only 4.5 % of specimens.

The analysis of crack initiation sites reveals a common trend across various loading conditions. Notably, crack initiation primarily occurs at the weld toe for both uniaxial and biaxial loading scenarios. This finding aligns with expectations, considering the well-known stress raising effects induced by the weld toe geometry, resulting in localised stress concentration during fatigue loading. However, under pure torsional fatigue loading, there is a significant shift in the primary site of crack initiation towards the weld start/stop position. Similarly, in biaxial fatigue loading, particularly with a λ of $\sqrt{3}$, failures predominantly occur at the weld start/stop position. This shift is significant, with 75 % of samples exhibiting a λ of $\sqrt{3}$ contributing to failures originating from this location. These experimental findings suggest a hypothesis that the combination of mode II loading or a λ of $\sqrt{3}$, along with the geometric features introduced by the weld start/stop position, creates a higher stress concentration region compared to the weld toe region [28,30,34,36]. The complexity of the localised weld start/stop geometry induces multiaxiality in stresses, leading to a highly damaging combined stress concentration effect, especially in the bulging region of the weld start/stop position. As for the relatively less common crack initiation sites, namely the weld itself and the aluminium HAZ, plausible explanations for failures occurring at the weld itself may be attributed to welding defects, such as lack of fusion between materials, presence of microcracks, and small pores, which ultimately resulted in the weakening of the weld and leads to early failure [6,18]. Regarding cracks originating from the aluminium HAZ, this could be due to very high mean stress torsional loads exceeding torsional limit of the aluminium material or it could be due to the

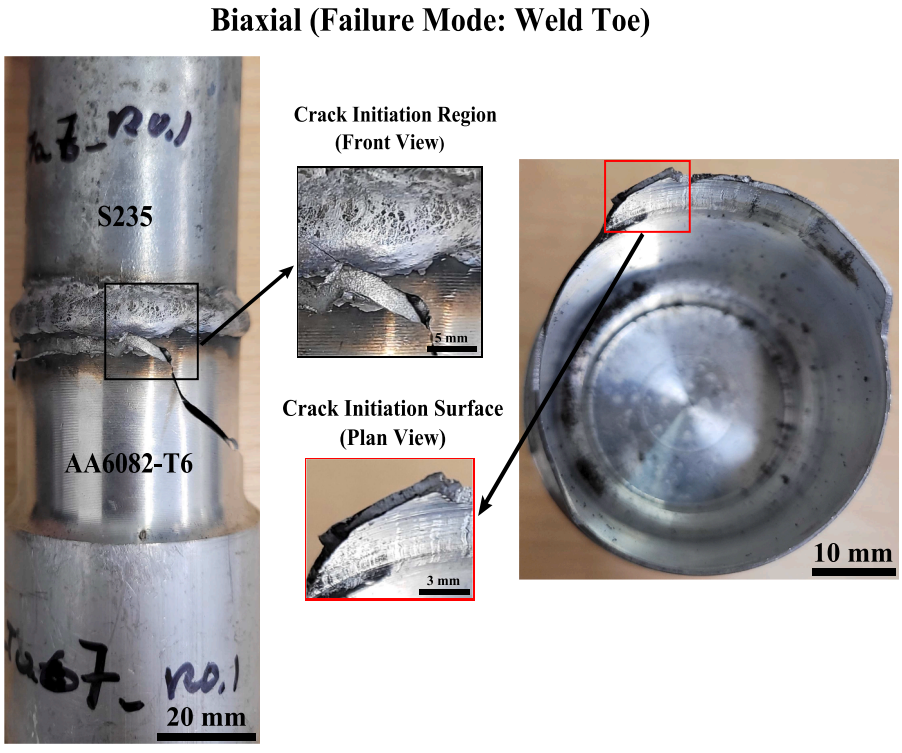

Fig. 9. Crack initiation under biaxial loading: (a) from weld toe, (b) from weld start/stop position, (c) from the weld itself, and (d) from the heat affected zone (HAZ) of aluminium.

critical weakening effect of the aluminium HAZ outweighing the stress concentration effect induced by the weld toe. It is worth noting that failures in this manner are relatively rare as under normal circumstances, the weld toe and weld start/stop positions tend to be more detrimental due to their higher stress raising effects.

3.2. Orientation of crack initiation and propagation planes

In addition to the analysis on crack initiation sites, the orientation of crack initiation and propagation was obtained using Image Processing Software Fiji, as outlined in Fig. 10. The crack path shown in Fig. 10 illustrates a biaxial in-phase fatigue loading case where the crack initiated from the weld toe. This case was chosen for its clear representation of initiation and propagation angles, unlike the zero-degree crack initiation angle seen in pure torsional cases. The angles obtained were designated as the experimental crack initiation angle, $A_{ini,exp}$ and experimental crack propagation angle, $A_{pro,exp}$, respectively. Notably, it was observed that the stage I crack initiation phase is comparatively shorter in uniaxial cases than in pure torsional and biaxial fatigue loading scenarios, as evidenced by the shorter stage I crack length. Consequently, the measurement of the initiation angle posed challenges in some instances due to the short crack length under uniaxial fatigue loading. Nevertheless, wherever possible, these experimental angles were measured and compared with the assumed critical plane orientation based on λ, which were derived from the Mohr's circle. These derived critical plane orientation were referred as the theoretical crack initiation, $A_{ini,theo}$ and crack propagation angle, $A_{pro,theo}$. While localised stress states induced by welds are crucial and often considered in complex welded joint geometries, nominal stress quantities are typically used as a baseline understanding and are widely adopted in the industry for design approximations, as recommended by the International Institute of Welding (IIW) and Eurocodes (ECs) [37–39]. To investigate the correlation between theoretical critical plane orientation and crack path angle under multiaxial fatigue loading in the examined specimen, the Mohr's circle was employed as a basic theoretical validation method. Although advanced critical plane approaches [36,40–43] are more suitable for detailed design stages, this straightforward Mohr's circle method was chosen to establish an initial understanding and identify potential correlations between crack path angle and theoretical critical plane orientation. Thus, nominal stress states were utilised in conjunction with the Mohr's circle approach to estimate the theoretical crack initiation and propagation angles.

In the medium to high cycle fatigue regime, it is assumed that *meso*-cracks in ductile materials primarily initiate due to shear stress [28,29,31,32,44]. This assumption finds support in experimental evidence indicating that cyclic shear stresses induce the formation of persistent slip bands (PSBs) and the initiation of *meso*-cracks. The application of fatigue loads results in intrusions and extrusions by the slip planes, leading to significant stress concentration effects that trigger the crack initiation phase [28,30,31,44,45]. These findings

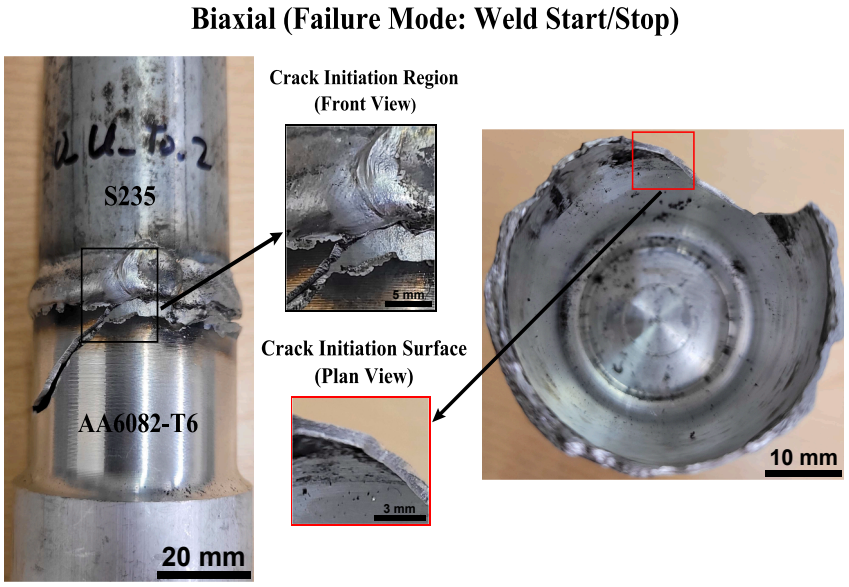

(b)

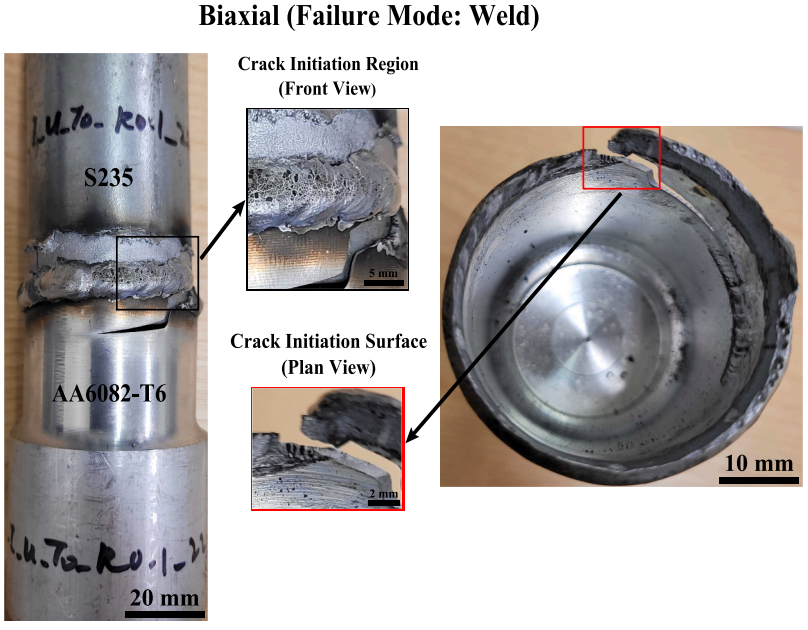

(c)

Fig. 9. (*continued*).

show the crucial role of the shear stress in initiating and propagating fatigue cracks, as evidenced by the presence of PSBs at a mesoscopic level. Consequently, the $A_{ini,theo}$ value derived from Mohr's circle corresponds to the plane orientation subjected to shear stress. Following crack initiation, the Stage II crack propagation phase is presumed to be governed by Mode I loading, indicative of maximum normal stress loading. During this phase, normal stresses facilitate the opening and propagation of the initiated crack until complete material separation [27–29,32,44]. Based on these observations, it can be hypothesised that the experimental orientation of the crack initiation plane should align with the orientation of the maximum shear stress plane, while the experimental crack propagation angle should correspond to the orientation of the maximum normal stress plane or maximum principal stress plane. To verify this hypothesis, the correlation between experimentally measured crack initiation plane orientation and theoretically derived orientation is depicted in Fig. 11a. Likewise, Fig. 11b illustrates the correlation between experimental and theoretical crack propagation plane orientation. The degree of correlation for both crack initiation and crack propagation angles is quantified using the calculated error, E, expressed as a percentage, as detailed in Eq. (2a) and Eq. (2b), respectively.

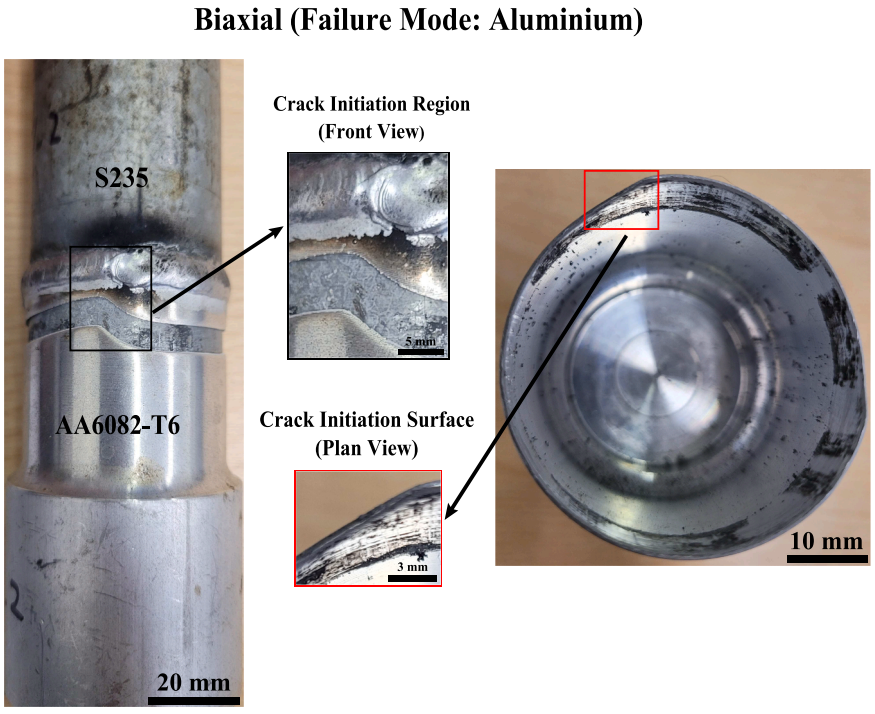

(d)

Fig. 9. (*continued*).

$$E(\%) = \frac{A_{ini,exp} - A_{ini,theo}}{A_{ini,theo}} \times 100 \tag{2a}$$

$$E(\%) = \frac{A_{pro,exp} - A_{pro,theo}}{A_{pro,theo}} \times 100 \tag{2b}$$

The percentage error method provides a clear visual representation of the correlation between experimentally measured and theoretically derived crack plane orientation in a log–log diagram. Additionally, alternative methods such as root mean square error (RMSE), mean absolute error (MAE), mean absolute relative error (MARE), and Nash Sutcliffe efficiency (NSE) are effective in demonstrating correlation. These methods are widely recognised for their ability to indicate prediction accuracy, especially in machine learning-based models, which are becoming increasingly popular as reported in [46].

To test one of the most popular prediction assessment models, the RMSE method was applied to verify the accuracy between experimental and theoretical initiation and propagation angles for this particular case, as shown in Equations (3a) and (3b), respectively.

$$RMSE(^\circ) = \sqrt{\sum_{i=1}^{n} \frac{(A_{ini,exp,i} - A_{ini,theo,i})^2}{n}} \tag{3a}$$

$$RMSE(^\circ) = \sqrt{\sum_{i=1}^{n} \frac{(A_{pro,exp,i} - A_{pro,theo,i})^2}{n}} \tag{3b}$$

Where n is the total number of observations. The resulting RMSE values were 8.9° for initiation angles and 8.3° for propagation angles.

In the context of uniaxial fatigue loading, cracks typically initiate around 45° and extend along the 0° axis in most instances. Under pure torsional fatigue loading, the crack initiation phase was seen to be relatively longer as compared to the uniaxial fatigue loading scenario. In this case, cracks initially form at the 0° maximum shear stress plane and branch into two opposite cracks during propagation phase, aligning closer to 45°, which corresponds to the maximum normal stress plane. This orientation appeared to be the same angles observed in out-of-phase constant amplitude loading scenarios. Conversely, for biaxial in-phase fatigue loading, crack initiation angles measure approximately 77° for a λ of 1 and 70° for λ of $\sqrt{3}$. Subsequently, crack propagation occurs at around 32° and 25°, respectively. It is worth mentioning that these observations were applicable to all crack initiation locations.

In Fig. 11a, a significant correlation is evident between the experimentally observed crack initiation plane orientation and its theoretically derived crack initiation plane orientation, with an error margin typically within ± 20 %. This high level of correlation is

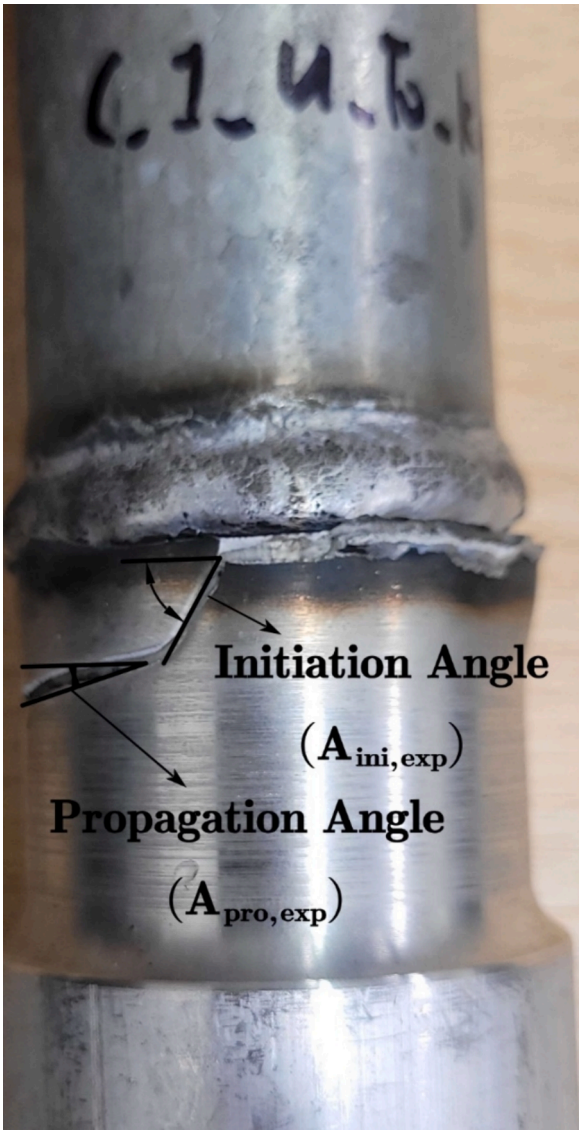

Fig. 10. Example illustrating the determination of experimental crack initiation angle, $A_{ini,exp}$ and experimental crack propagation angle, $A_{pro,exp}$ under biaxial in-phase fatigue loading.

especially noteworthy, considering the number of random factors including potential microstructural defects and intricate local weld geometries, that could influence the crack initiation plane orientation. It strongly suggests that by focusing on the analysed hybrid aluminium to steel joints, the crack initiation phase is predominantly influenced by shear stresses, closely aligning with the orientation of the maximum shear stress plane. Examining the correlation between experimental and theoretical crack propagation angles shown in Fig. 11b, reveals that most data points fall within a ± 30 % error margin, indicating a reasonable correlation, despite the 10 % increase in error compared to the initiation phase. This slight rise in error is likely due to the complex geometry and the influence of microstructural hard inclusions, causing deviations in the crack propagation path. Nevertheless, this analysis underscores the critical role of normal stresses in governing the stage II crack propagation phase.

4. Conclusions

Based on the crack path analysis conducted on the hybrid aluminium-to-steel welded joints, the following conclusions can be drawn:

a) Cracks consistently initiate from a singular point, irrespective of failure mode, fatigue loading type or level of stress amplitudes.
b) Four primary crack initiation locations were identified: the weld toe, weld start/stop position, weld itself, and the aluminium HAZ.

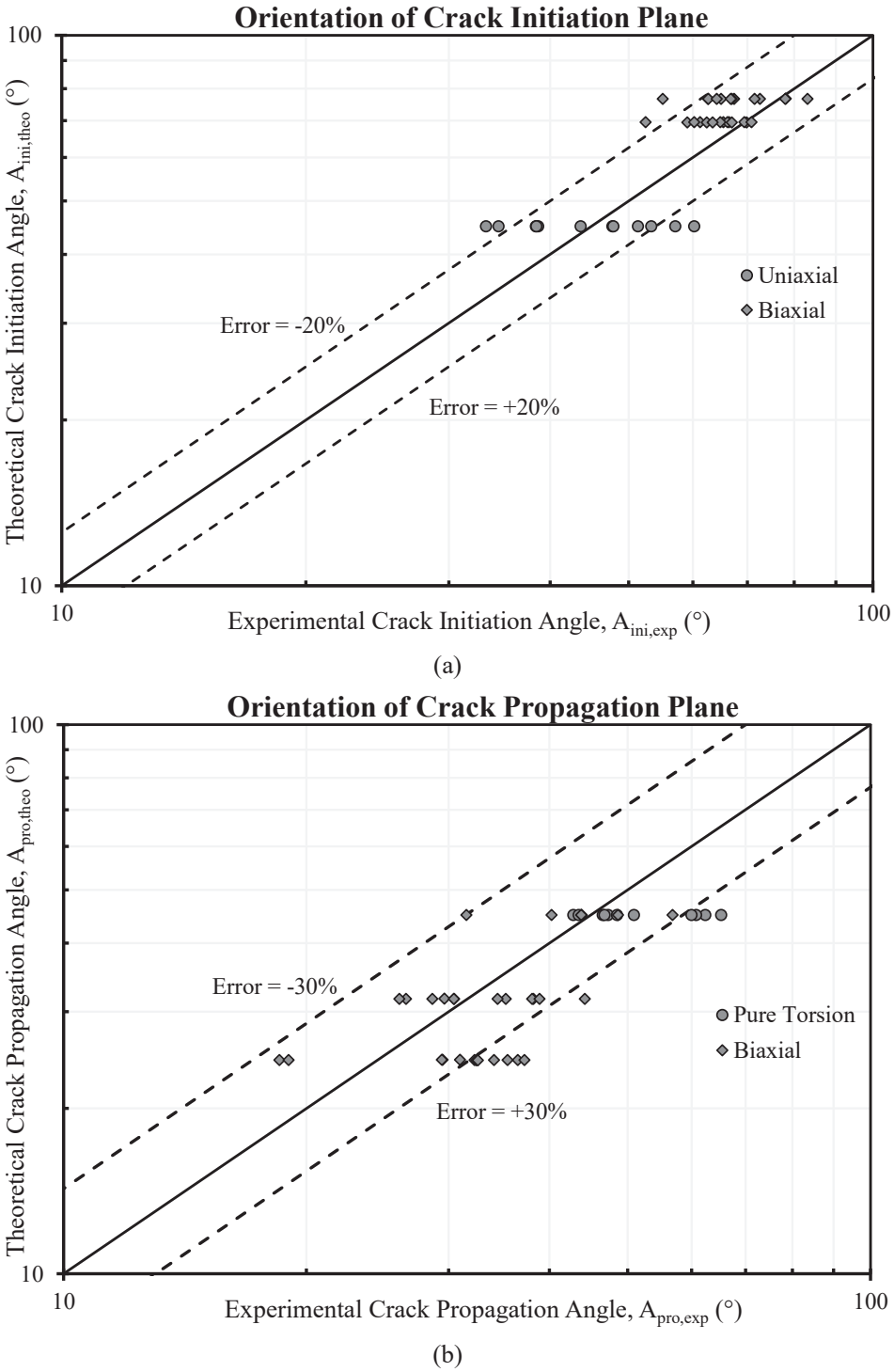

Fig. 11. Correlation between experimental and theoretical crack plane angles: (a) crack initiation angles ($A_{ini,exp}$ vs $A_{ini,theo}$) and (b) crack propagation angles ($A_{pro,exp}$ vs $A_{pro,theo}$).

c) The weld toe region predominantly served as the crack initiation site, especially evident under uniaxial and biaxial fatigue loading, with 75 % and 55 % of samples exhibiting failure from this location, respectively.
d) Cracks originating from the weld itself were relatively rare, indicating the effectiveness of EWM cold arc technology in welding thin dissimilar aluminium-to-steel connections. Conversely, crack initiation from the aluminium HAZ was the least common, suggesting

that stress concentration effects due to weld geometry are more detrimental than the weakening effect caused by the HAZ in the aluminium region.

e) Crack plane orientation analysis confirmed that the crack initiation phase is governed by shear stresses, while the crack propagation phase is influenced by normal stresses. Experimental crack plane orientation closely matched the theoretical orientation of the maximum shear stress plane and maximum normal stress plane, with errors predominantly within ± 20 % for the crack initiation angle and within ± 30 % for the crack propagation angle.

CRediT authorship contribution statement

Chin Tze Ng: Writing – original draft, Investigation, Formal analysis. **Luca Susmel:** Writing – review & editing, Supervision, Methodology, Conceptualization.

Declaration of competing interest

The authors declare that they have no known competing financial interests or personal relationships that could have appeared to influence the work reported in this paper.

Data availability

Data will be made available on request.

Acknowledgements

This research was supported by the University of Sheffield Faculty of Engineering University Research Scholarship. The authors would like to extend their sincere gratitude to technicians Paul Blackbourn, Kieren O. Howarth, Richard Kay, Chris Todd, Billy Fidell, and Luke R. Callaghan for their invaluable assistance in the manufacturing of specimens and ensuring the smooth execution of fatigue testing.

References

[1] A. Gullino, P. Matteis, F. D'Aiuto, Review of aluminum-to-steel welding technologies for car-body applications, Metals (basel). 9 (2019) 315.
[2] S. Meco, G. Pardal, S. Ganguly, S. Williams, N. McPherson, Application of laser in seam welding of dissimilar steel to aluminium joints for thick structural components, Opt. Lasers Eng. 67 (2015) 22–30.
[3] P. Kah, R. Suoranta, J. Martikainen, Advanced gas metal arc welding processes, Int. J. Adv. Manuf. Technol. 67 (2013) 655–674.
[4] H.R. Shahverdi, M.R. Ghomashchi, S. Shabestari, J. Hejazi, Microstructural analysis of interfacial reaction between molten aluminium and solid iron, J. Mater. Process. Technol. 124 (2002) 345–352.
[5] S.F. Goecke, Low energy arc joining process for materials sensitive to heat, EWM Hightec Weld. Gmbh. 3 (2005).
[6] I. Al Zamzami, V. Di Cocco, J.B. Davison, F. Iacoviello, L. Susmel, Static strength and design of aluminium-to-steel thin welded joints, Weld. World. 62 (2018) 1255–1272, https://doi.org/10.1007/s40194-018-0634-2.
[7] K. Bouche, F. Barbier, A. Coulet, Intermetallic compound layer growth between solid iron and molten aluminium, Mater. Sci. Eng. A. 249 (1998) 167–175.
[8] M.M. Atabaki, M. Nikodinovski, P. Chenier, J. Ma, M. Harooni, R. Kovacevic, Welding of aluminum alloys to steels: an overview, J. Manuf. Sci. Prod. 14 (2014) 59–78.
[9] G. Qin, Y. Su, S. Wang, Microstructures and properties of welded joint of aluminum alloy to galvanized steel by Nd: YAG laser+ MIG arc hybrid brazing-fusion welding, Trans. Nonferrous Met. Soc. China. 24 (2014) 989–995.
[10] R. Cao, J.H. Sun, J.H. Chen, P.-C. Wang, Cold metal transfer joining of aluminum AA6061-T6-to-galvanized boron steel, J. Manuf. Sci. Eng. 136 (2014) 051015.
[11] K. Kimapong, T. Watanabe, Lap joint of A5083 aluminum alloy and SS400 steel by friction stir welding, Mater. Trans. 46 (2005) 835–841.
[12] R.W. Richards, R.D. Jones, P.D. Clements, H. Clarke, Metallurgy of continuous hot dip aluminizing, Int. Mater. Rev. 39 (1994) 191–212.
[13] Y. Liu, R. Liu, Z. Zhu, Y. Li, H. Chen, Fracture mechanism of aluminum/steel laser-arc welded-brazed joints during quasi-static tensile and dynamic fatigue tests, Eng. Fail. Anal. 152 (2023) 107461.
[14] A. Kalinenko, I. Zuiko, S. Malopheyev, S. Mironov, R. Kaibyshev, Dissimilar friction-stir welding of aluminum alloys 2519, 6061, and 7050 using an additively-manufactured tool, Eng. Fail. Anal. 156 (2024) 107851.
[15] H.T. Wang, G.Z. Wang, F.Z. Xuan, S.T. Tu, An experimental investigation of local fracture resistance and crack growth paths in a dissimilar metal welded joint, Mater. Des. 44 (2013) 179–189.
[16] R.D. Caligiuri, Critical crack path assessments in failure investigations, Frat. Ed Integrità Strutt. 9 (2015).
[17] E. Maggiolini, R. Tovo, L. Susmel, M.N. James, D.G. Hattingh, Crack path and fracture analysis in FSW of small diameter 6082–T6 aluminium tubes under tension–torsion loading, Int. J. Fatigue. 92 (2016) 478–487.
[18] W. Shin, K.-H. Chang, S. Muzaffer, Fatigue analysis of cruciform welded joint with weld penetration defects, Eng. Fail. Anal. 120 (2021) 105111.
[19] H. Amstutz, K. Störzel, T. Seeger, Fatigue crack growth of a welded tube–flange connection under bending and torsional loading, Fatigue Fract. Eng. Mater. Struct. 24 (2001) 357–368.
[20] H. Liu, S. Yang, C. Xie, Q. Zhang, Y. Cao, Mechanisms of fatigue crack initiation and propagation in 6005A CMT welded joint, J. Alloys Compd. 741 (2018) 188–196.
[21] Z. Zhang, Quantitative characterization on fatigue fracture features of A6005 aluminum alloy welded joints, Eng. Fail. Anal. 129 (2021) 105687.
[22] I. Al Zamzami, L. Susmel, On the use of hot-spot stresses, effective notch stresses and the Point Method to estimate lifetime of inclined welds subjected to uniaxial fatigue loading, Int. J. Fatigue. 117 (2018) 432–449, https://doi.org/10.1016/j.ijfatigue.2018.08.032.
[23] F. Yousefi, M. Witt, H. Zenner, Fatigue strength of welded joints under multiaxial loading: experiments and calculations, Fatigue Fract. Eng. Mater. Struct. 24 (2001) 339–355.
[24] L. Susmel, Three different ways of using the Modified Wöhler Curve Method to perform the multiaxial fatigue assessment of steel and aluminium welded joints, Eng. Fail. Anal. 16 (2009) 1074–1089, https://doi.org/10.1016/j.engfailanal.2008.05.016.
[25] K.A. Macdonald, P.J. Haagensen, Fatigue of welded aluminium hollow section profiles, Eng. Fail. Anal. 16 (2009) 254–261.

[26] ASTM E739-10, ASTM E739-10 Standard Practice for Statistical Analysis of Linear Or Linearized Stress-Life (SN) and Strain-Life (ε-N) Fatigue Data, in: ASTM, 2010.
[27] L.P. Pook, On fatigue crack paths, Int. J. Fatigue. 17 (1995) 5–13.
[28] L. Susmel, Multiaxial notch fatigue, Elsevier, 2009.
[29] D.F. Socie, Multiaxial fatigue damage models, (1987).
[30] S. Suresh, Fatigue of materials, Cambridge University Press, 1998.
[31] M.D. Sangid, The physics of fatigue crack initiation, Int. J. Fatigue. 57 (2013) 58–72.
[32] G. Totten, Fatigue crack propagation, Adv. Mater. Process. 166 (2008) 39–42.
[33] L. Reis, B. Li, M. De Freitas, Analytical and experimental studies on fatigue crack path under complex multi-axial loading, Fatigue Fract. Eng. Mater. Struct. 29 (2006) 281–289.
[34] J. Schijve, Fatigue of structures and materials, Springer, 2009.
[35] K. Macdonald, Fracture and fatigue of welded joints and structures, Elsevier, 2011.
[36] M. Kueppers, C.M. Sonsino, Critical plane approach for the assessment of the fatigue behaviour of welded aluminium under multiaxial loading, Fatigue Fract. Eng. Mater. Struct. 26 (2003) 507–513.
[37] A. Hobbacher, Recommendations for fatigue design of welded joints and components, Springer, 2016.
[38] Anon, Eurocode 3: Design of steel structures — Part 1-9: Fatigue, 2005.
[39] Anon, Eurocode 9: Design of aluminium structures — Part 1-3: Structures susceptible to fatigue, 2007.
[40] A. Carpinteri, A. Spagnoli, S. Vantadori, Multiaxial fatigue life estimation in welded joints using the critical plane approach, Int. J. Fatigue. 31 (2009) 188–196.
[41] L. Susmel, Four stress analysis strategies to use the Modified Wöhler Curve Method to perform the fatigue assessment of weldments subjected to constant and variable amplitude multiaxial fatigue loading, Int. J. Fatigue. 67 (2014) 38–54, https://doi.org/10.1016/j.ijfatigue.2013.12.001.
[42] M.M. Pedersen, Multiaxial fatigue assessment of welded joints using the notch stress approach, Int. J. Fatigue. 83 (2016) 269–279, https://doi.org/10.1016/J.IJFATIGUE.2015.10.021.
[43] L. Susmel, A simple and efficient numerical algorithm to determine the orientation of the critical plane in multiaxial fatigue problems, Int. J. Fatigue. 32 (2010) 1875–1883, https://doi.org/10.1016/j.ijfatigue.2010.05.004.
[44] M.W. Brown, K.J. Miller, Initiation and growth of cracks in biaxial fatigue, Fatigue Fract. Eng. Mater. Struct. 1 (1979) 231–246.
[45] M.R. Lin, M.E. Fine, T. Mura, Fatigue crack initiation on slip bands: theory and experiment, Acta Metall. 34 (1986) 619–628.
[46] S.-P. Zhu, X. Niu, B. Keshtegar, C. Luo, M. Bagheri, Machine learning-based probabilistic fatigue assessment of turbine bladed disks under multisource uncertainties, Int. J. Struct. Integr. 14 (2023) 1000–1024.